Research Article | Vol. 11, No. 9 / 1 Sep 2021 / Optical Materials Express 3056
Optical Materials EXPRESS

Laser cladding of transparent fused silica glass using sub-µm powder

PAWEL MANIEWSKI,* FREDRIK LAURELL, AND MICHAEL FOKINE

Laser Physics Group, School of Engineering Science, KTH Royal Institute of Technology, Stockholm, Sweden
*pawelma@kth.se

Abstract: Fused silica glass is a commonly used high-performance material. However, due to the high temperature necessary for its production, manufacturing can also be challenging and costly. An attractive approach is additive manufacturing through laser cladding. Laser cladding of transparent fused silica was achieved using a CO_2-laser to locally melt the substrate while injecting a stream of fumed silica glass powder into the melt-pool. By the described technique, it is possible to manufacture fully sintered silica glass with deposition rate up to 29 mm^3/min. In this work we have studied deposition dynamics and influence of different process parameters on the final deposition quality.

1. Introduction

Additive manufacturing (AM) technologies have seen a rapid development in recent decades with an increasing number of materials being made available. The most desirable benefits of AM, also referred to as 3D printing, include flexibility in design and geometry and simplified tailoring of customized prints, reduced material waste, and the ability to fabricate complex structures, often not possible using traditional subtractive manufacturing. While ideal for prototyping, AM is now increasingly being used in production due to advances in performance and printing speed [1]. Most commonly used materials today include metals and alloys, polymers and composites, and ceramics [2]. Glass is a material used in all parts of society and is commonly associated with high mechanical, chemical and thermal stability. High optical transparency, and ability to refractive index engineering, makes glass a highly versatile high-performance material used, e.g., for optics and windows, containers for nuclear waste [3], micro-fluidic platforms [4] and optical fibers.

While metals and polymers have seen a rapid development, progress in glass AM, especially fused silica AM techniques, has been slow. The high stability of fused silica is due to the strong covalent Si-O bonds forming the glass network. A consequence of the strong bonding is that high temperatures are often required for fabrication and processing. Combined with the fragile nature of glass, developing glass AM techniques has been challenging. Today there are few reports on glass AM techniques, or glass 3D printing, including extrusion printing [5], fiber-feeding printing [6], selective laser sintering and melting (SLS and SLM) [7], stereolithography with necessity of oven sintering [8]. Among different methods of AM, powder-based techniques are characterized by the high flexibility [9]. Here one of the ways of powder delivery, the powder bed method, is through layer-by-layer powder deposition of specified layer thickness. By scanning the laser beam across each layer local sintering occur, subsequently forming a solid geometry on which the next powder layer is deposited. Removing unsintered powder from the working chamber once the build is complete, the solid manufactured object is revealed. One drawback of the powder bed method in glass manufacturing is that printed objects tend to have a porous structure due to incomplete sintering/melting of the powder, due to a significant decrease in volume as the top layer of the glass powder is sintered. This results in formation of voids as the high viscosity of the molten glass traps gas within the printed object [10]. The resulting object often requires

#433734 https://doi.org/10.1364/OME.433734
Journal © 2021 Received 9 Jun 2021; revised 30 Jul 2021; accepted 1 Aug 2021; published 23 Aug 2021

Optical Materials EXPRESS

thermal post-processing for complete sintering with subsequent further reduction in volume [11]. This effect can partly be reduced by using another powder-based technique, laser cladding (LC). Here a laser beam is used to irradiate the solid substrate, creating a localized melt pool. Powder is then injected into the melt pool, effectively adding material to the build. Material is added layer-by-layer by traversing the melt pool, while adding powder [9]. Although the outer surfaces tend to be rough, due to incomplete sintering of excess powder, internal voids can be reduced as long as there is complete melting/sintering of the particles within the melt pool. An attractive feature with LC is the ability to change the material composition of the manufactured part during fabrication [12], which is highly desirable for applications in photonics. Glass and glass ceramic scaffolds for use towards, e.g., bone regeneration, has also been reported using LC [13].

A major challenge in LC, however, is the shadowing effect, i.e., when the injected powder interacts with the irradiating beam, effectively shadowing the substrate due to absorption and scattering [14]. Any variations in powder flow dynamics will result in unstable temperature and size of the melt pool, and subsequently reduced control and reproducibility of the deposition process. Partial sintering of particles prior to reaching the substrate and melt pool can also give rise to incomplete sintering, resulting in formation of voids within the build [15]. In previous work [16] we proposed to use powder particle size much smaller than the laser wavelength in order to mitigate shadowing effects during LC.

In this work, we investigate the deposition dynamics when using sub-micron silica powder in LC. A CO_2-laser operating at 10.6 µm was used to heat a quartz glass substrate. Injecting fumed silica, having sub-micron particle size, absorption and scattering of the laser beam was reduced significantly increasing stability of the deposition process. An innovative nozzle design including integrated shaping gas was used to reduce the divergence of the injected powder cone, enabling a longer working distance between powder nozzle and melt pool. Deposition of fully sintered glass was successfully achieved with deposition rates up to 29 mm^3/min, with a powder efficiency up to 30% by weight. Fully sintered and transparent, glass deposition with a single layer height of up to 150 µm was demonstrated. Different geometries such as trenches, single tracks, coatings, and walls were fabricated and analyzed to better understand the deposition dynamics.

2. Use of sub-µm powders in the laser cladding of glass

Successful fusing of the glass powder with the substrate is closely related to the material properties (viscosity, surface energy), the temperature and size of the melt pool, as well as the temperature dynamics of the molten glass [9]. In LC or SLM of glass powders, commonly used particle diameters are in the range from 10 µm to 250 µm [7,13,17]. Here Nd:YAG lasers operating at 1064 nm, and CO_2 lasers at 10,6 µm, were used for glass powder sintering [13,15,18]. In LC the melt pool is formed by absorption of energy delivered to the substrate by the scanning laser beam. The high absorption in silica at $\lambda = 10.6$ µm, with an absorption depth in the order of a few µm, makes CO_2 lasers particularly suitable [19]. To achieve a stable temperature and size of the melt pool the irradiating laser beam should be transmitted through the stream of injected particles with minimum interaction. The light-particle interaction, in this case, include transmission, reflection, refraction, absorption, and scattering. Here scattering and absorption have dominating contribution to the shadowing effect [14,20]. To analyze these contributions we can look at scattering and absorption related effects separately. A simplified sketch of light scattering is shown in Fig. 1.

The amount of light scattered from the particle depends on polarization, wavelength, and material properties of the sphere, or more specifically the physical size and the dielectric constant (refractive index, absorption). There are different regimes of scattering, which depends on the particle size and the wavelength [21,22]. A dimensionless size parameter, $x = \pi D/\lambda$, where D is the particle diameter and λ is the wavelength of light used to distinguish different scattering regimes [22]. For particles with a size parameter of $x \geq 100$ geometrical optics applies. Scattering

Optical Materials EXPRESS

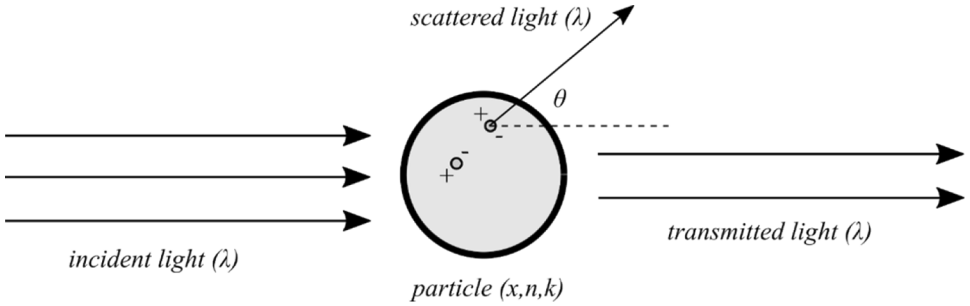

Fig. 1. Scattering of light by induced dipoles in a spherical particle.

is described by Mie theory in the range of $0.1 < x < 100$. For smaller particles, with a size parameter below $x \sim 0.1$, Rayleigh scattering approximation can be used. The different scattering regions are shown in Fig. 2. The particle diameter of fumed silica used in this work, approximately 0.01 - 0.05μm, is indicated in Fig. 2, together with the wavelength of the laser used in our experiments *($\lambda = 10.6$ μm)*, indicating that we are operating in the Rayleigh scattering regime.

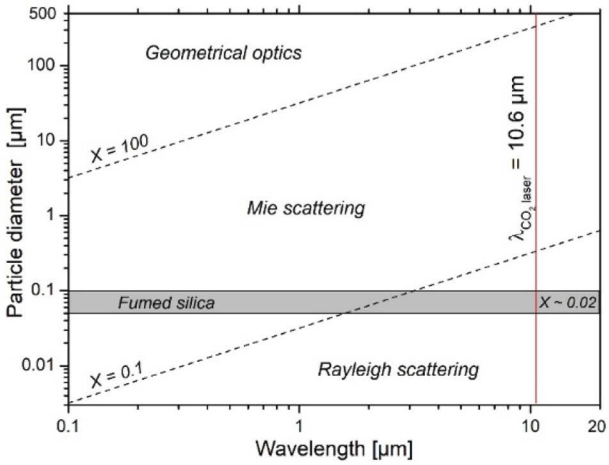

Fig. 2. Particle diameter vs. wavelength, where different scattering regions are labeled related to the size parameter (X). The grey area indicates the particle size distribution of fumed silica. The vertical red line corresponds to the wavelength of the CO_2-laser used in this work.

Our calculations on the magnitude of scattering as a function of particle size are based on the theoretical work of Mie [21]. Numerical algorithm for Mie scattering calculations was originally described and demonstrated in Fortran by Wiscombe [23], later translated to Python by Prahl [24]. The Python version of the code, and the silica properties *($n(\lambda=10,6$ μm$) = 2.025$ k=- 0.021777)* reported in [19] were used for the simulations in this work. For simplicity we considered unpolarised light interacting with the glass powder. The calculated values for scattered intensity, $p(\theta)$, is given by:

$$p(\theta) = \frac{|S_1|^2 + |S_2|^2}{\pi x^2 Q_{scat}}, \tag{1}$$

where S_1 and S_2 are the amplitude functions for perpendicular and parallel polarization respectively, and Q_{scat} is a dimensionless efficiency factor defined as the ratio between geometrical and

Optical Materials EXPRESS

scattering cross-sections [25]. The scattered light intensity for different particle sizes, calculated as a function of scattering angle and a wavelength of 10.6 μm, is shown in Fig. 3.

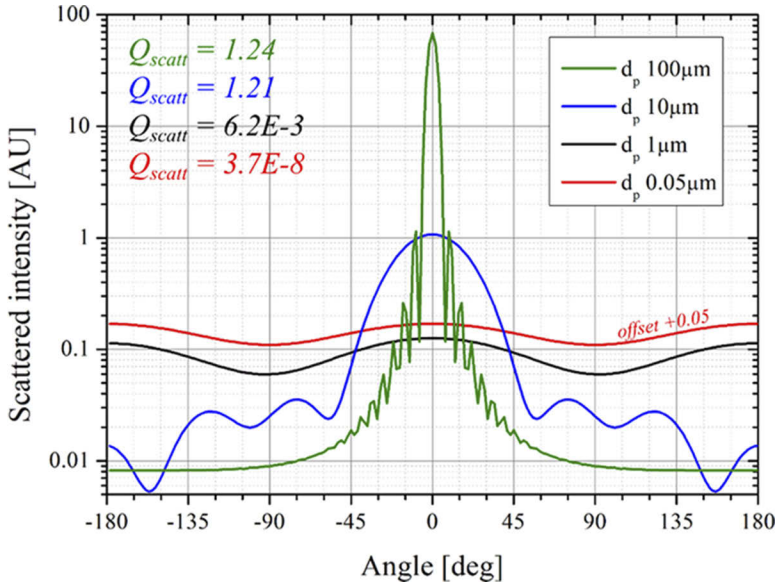

Fig. 3. Magnitude of scattering as a function of scattering angle for different glass powder diameters (d_p = 0.05, 1, 10, 100 μm), a laser wavelength of λ = 10.6 μm, and dielectric constants of n = 2.025, and k = 0.021777 [19].

For larger particles (d_p = 10 μm and 100 μm) interaction in the Mie regime results in a high scattering efficiency within a narrow range of forward scattering angles, as can be seen in Fig. 3. For very small particles *(x~0.02, d_p<1 μm)*, within the Rayleigh regime, scattering result in much wider scattering angles, while the scattering efficiency is significantly lower. This can be understood from the scattering coefficient (σ_s), which is proportional to $\sigma_s \propto r^6\lambda^{-4}$ [22] where r is the particle radius and λ is the wavelength of light.

Considering the data shown in Fig. 3, the contribution of scattering to the shadowing effect can be viewed as minor. Although scattering efficiency for large particles is significantly higher, the scattering angle is small, which could lead to a marginal increase of the size of the melt pool. Scattering is therefore expected to have a low impact on the heating dynamics and the deposition efficiency during LC. Particle absorption, however, is likely to have a larger impact. In the Rayleigh regime the absorption cross-section is given by $C_a \propto r^3\lambda^{-1}$ [22]. The reduction of the absorption coefficient, defined as $_a = NC_a$, where N is the number of particles per volume [22,25], scales with *r3* and is related to the volume of the absorbing particles. The total attenuation of the incident laser beam through a uniformly distributed powder stream can described by the Beer-Lambert law:

$$\frac{I}{I_0} = e^{-\varepsilon_e L}, \tag{2}$$

where L is the optical interaction length and the extinction coefficient εe, which is a function of the number of particles per volume *(N)*, scattering and absorption, given by $\varepsilon_e = N(C_s + C_a)$. The dominating attenuation mechanism in the Rayleigh regime is absorption. As shown in Fig. 4 the absorption coefficient for smaller particles is several orders of magnitude larger compared to the scattering coefficient.

As the particles absorb light, their temperature increases. With sufficient laser power, the temperature of the particles can become high enough to start fusing together forming larger,

Optical Materials EXPRESS

partly sintered clusters with irregular shape, as illustrated in Fig. 5. Once deposited in the melt pool, if not fully melted these partly sintered clusters may result in void formation within the manufactured object.

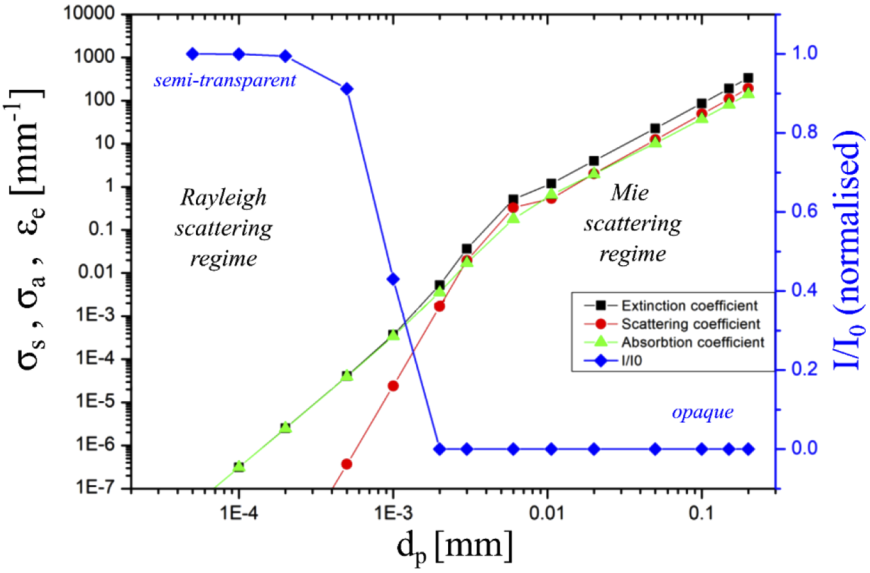

Fig. 4. Calculated scattering (σ_s, *red*), and absorption (σ_a, green) coefficients for a wavelength of λ=10.6 µm, as a function of particle diameter for silica glass powder, including the normalized light attenuation (I/I_0, blue).

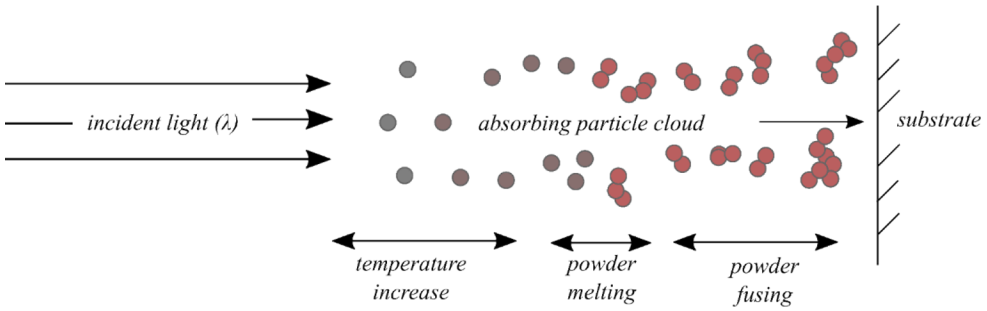

Fig. 5. Schematic of absorption induced clustering of powder.

Fumed silica, having sub-micron particle size, is characterized by high purity with a non-porous structure. With a particle size in the range 0.05 µm to 0.1 µm, light interaction at a wavelength of $\lambda = 10.6$ µm is described by Rayleigh scattering. The model used for calculations treats the particles as a perfect spheres. Real particles can contain surface defects and have uneven shape. These properties, however, are not likely to have any significant impact on over-all light-matter interaction due to the combination of long laser wavelength and small size parameter. For fumed silica particles the scattering angle distribution is large, however the extinction coefficient very low. With an absorption depth in silica on the order of a few µm at $\lambda = 10.6$ µm [19], fumed silica particles can be considered to be semi-transparent. The semi-transparency and the small absorption cross-section therefore limit the temperature increase of the particles prior to reaching the melt pool. Therefore, the combined effects of using a CO2-laser with fumed silica glass

Optical Materials EXPRESS

powder, significantly reduces the shadowing effect while avoiding partial sintering of airborne particles. The injected particles should be fused together with the substrate upon contact with the laser induced hot zone. This should result in a more stable LC process with deposited glass containing fewer voids and inclusions.

3. Experimental setup

The experimental LC setup, developed in house, was made up of three separate parts: laser and beam steering optics, motorized stages for translation of glass substrate, and powder nozzle with powder feeding system. A schematic of the optical setup is shown in Fig. 6. A linearly polarized CO2-laser operating at a wavelength of $\lambda = 10.6$ µm, having a Gaussian beam (*M2 = 1.1*), with a maximum output power of 50 W was used (ULR OEM 50W, Universal Laser Systems). Silver coated mirrors (ThorLabs Inc.) were used for beam steering. The laser beam was focused using a spherical, AR-coated ZnSe lens (ThorLabs Inc.), with a focal length of 40 mm. The lens was mounted on a motorized stage (*z-axis*) to adjust the focal position depending on the substrate position or layer height. The glass substrate was mounted on motorized stages for two axis translation (*x- and y-axes*). The powder nozzle was positioned at an angle of 45° relative to the laser beam, as shown in Fig. 7. The nozzle was mounted on the motorized *z-axis* stage using an additional mechanical translation stage, allowing the position of the nozzle to be easily changed. The 100 mm long nozzle (custom made co-axial needle by Ramé-Hart Instrument Co.) was constructed of two equal length co-axial stainless-steel tubes (wall thickness 0.4 mm) with inner diameters of 1.04 mm and 3 mm, as can be seen in Fig. 7. Glass powder was fed through the inner tube while shaping gas (dry air, N_2+21%O_2) was purged through to the outer tube, and the flow rate was controlled using separate flow regulators.

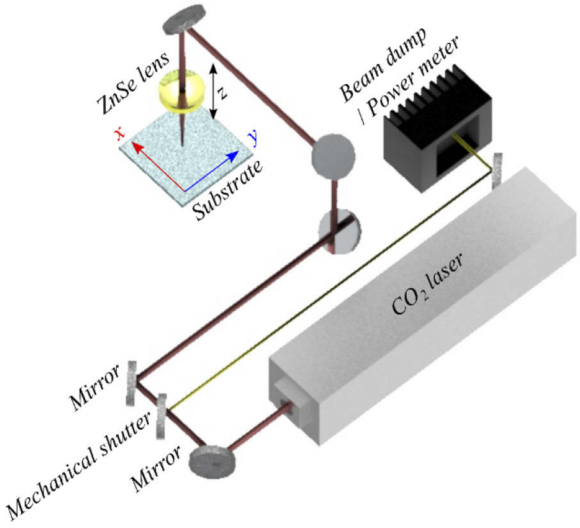

Fig. 6. Schematic of the experimental set-up, including CO_2-laser, beam steering mirrors, mechanical shutter, beam dump, movable ZnSe focusing lens, and glass substrate.

A powder feeder (MARK XV, Powder Feed Dynamics Inc.) was used to transport powder to the optical setup and the powder nozzle. Powder was guided through grounded, antistatic polyurethane tubing to minimize electrostatic effects. The powder canister equipped with a single helical conveyor (*feeding screw*) had a powder capacity of approximately 4000 cm^3, with powder injected into the carrier gas stream via a carburetor. Dry air (N_2+21%O_2) was used as the carrier gas. Due to the low volume density when using sub-micron powders the feeding

Optical Materials EXPRESS

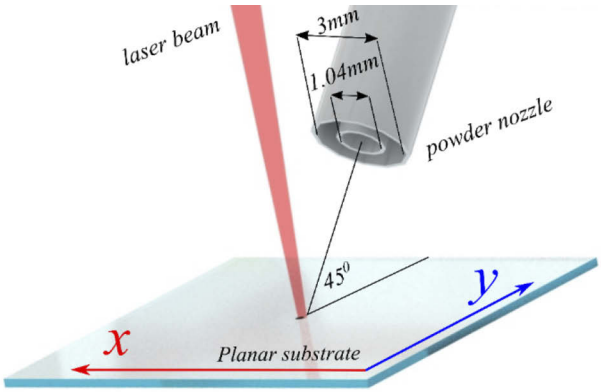

Fig. 7. Schematic of the powder feeding nozzle alignment for planar substrates.

screw mechanism, relying on gravitational flow, was insufficient, resulting in unstable powder feeding. This was solved by modifying the feeder by introducing a slight over-pressure (approx. 1.4 Bar) in the powder canister, combined with a relatively slow rotation of the feeding screw (32 RPM), located at the bottom of the container. Powder feeding is therefore achieved through a combination of screw feeding and forced carrier gas flow. The modified design significantly improved the feeding stability. The feeding rate was subsequently calibrated in range of 0.4–1.5 g/min [16]. Fumed silica is hygroscopic, and absorption of water can lead to formation of clusters affecting the flow dynamics, which can result in clogging of the tubing as well as the nozzle. The powder canister was therefore equipped with a heating blanket (Silicone foil heater, IHP AB) to reduce the water content and keep the powder dry. Furthermore, to minimize the water content, in particular when using fumed silica, the powder was pre-processed by baking at a temperature of 105°C for at least 48h prior to use.

3.1. Evaluation of the nozzle design

To examine the impact of shaping gas on the injected powder distribution, several different flow rates of the shaping gas were investigated. Dry air (N_2+21%O_2) was used both as carrier (CG) and shaping gas (SG).

A red laser diode ($\lambda = 0.65$ µm) with a line focus was aligned along the axial direction of the nozzle. This probe beam was launched from right in Fig. 8(a), with the powder nozzle visible in the top-right corner. The similar dimensions of the wavelength of the diode laser and particle diameter resulted in strong scattering, allowing visualization of the powder stream. For the analysis we assume that the measured scattering intensity is directly proportional to the particle concentration. Images of the powder stream distribution exiting the nozzle was collected using a CCD camera (ThorLabs Inc.) positioned perpendicular to the laser beam. Images were separated into RGB channels, and the red monochromatic image was used to analyze the powder stream distribution. Figure 8(a) shows a typical image with the measurement points at 3 mm intervals from the nozzle indicated. Here the image negative is shown for enhanced clarity. Using image processing the radial intensity distribution of the scattered light was extracted, and Fig. 8(b) shows the evolution of the powder distribution exiting the nozzle for the different measurement points.

The CG flow rate was constant and set to 4 L/min for all experiments. To analyze the effect of the SG, the powder distribution was measured for SG flow rates of 0, 4 and 10 L/min. A SG flow of 0 L/min corresponds to commonly used single off-axis nozzle LC systems. To compare the results for different SG flow rates the full-width-half-maximum (FWHM) of the powder

Optical Materials EXPRESS

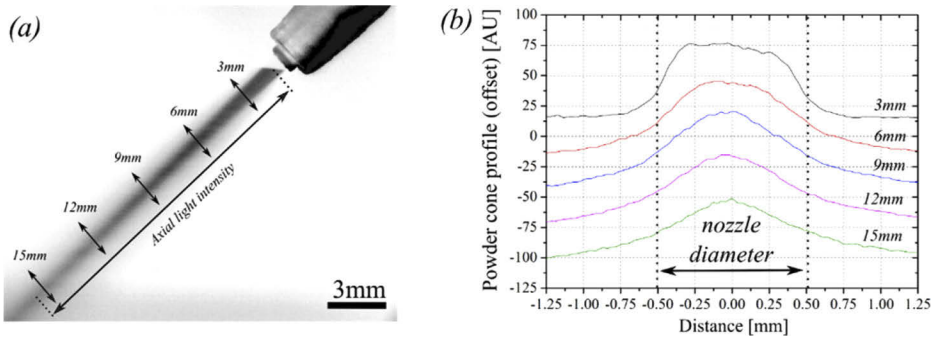

Fig. 8. Image (a) of the nozzle and the scattered light from the powder stream, and (b) the corresponding light distribution measurements, which have been offset for clarity.

distribution was measured at the different measurement positions. The widths, and scattered light along the injection, both normalized to the inner diameter of the nozzle (1.04 mm), are shown in Fig. 9(a).

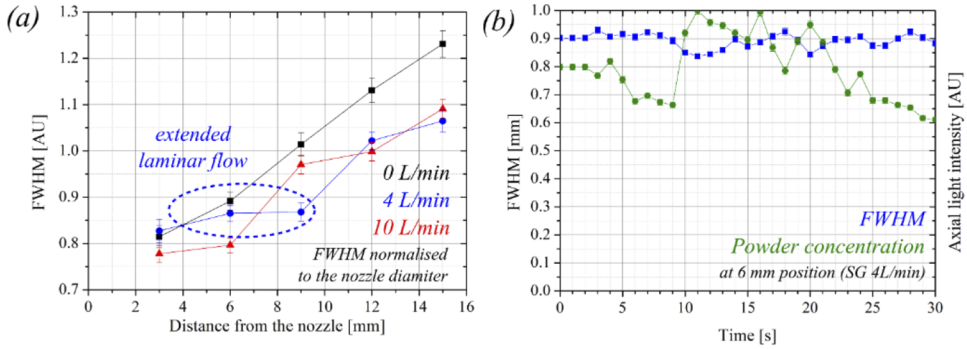

Fig. 9. The impact (a) of shaping gas (SG) on the powder cone shape was investigated for three different flow rates of the shaping gas, together with the short-term stability of the powder injection (b).

Here it is seen that a 1:1 ratio of SG:CG flow rates extends the laminar region of the powder flow from around 6 mm to approximately 9 mm, enabling a longer working distance between the nozzle and the melt pool. With a powder nozzle placed in relatively short distance from laser induced hot zone, there is a risk of overheating the nozzle that may affect its geometry, lifetime and lead to early failure. Thus, using a longer working distance is preferable in order to reduce heating of the nozzle and reduce the complexity of integrating the nozzle with an additional cooling system.

To evaluate the short-term stability of the powder distribution and powder feeding stability, images taken at 1 second intervals were analyzed. The results, plotted in Fig. 9(b) shows the measured FWHM and normalized axial light intensity, proportional to the powder concentration, measured at a distance of 6 mm from the nozzle using a SG flow rate of 4 L/min. While the shape of the injection remains stable in time (+/- 5%), variations in powder feeding rate is clearly seen (+/- 20%).

Optical Materials EXPRESS

3.2. Sample preparation and characterization

For this study we used 1 mm thick flat polished fused quartz wafers as substrates. Geometrical characterization of printed structures was performed using an optical microscope (Nikon Eclipse LV100) equipped with a CCD camera. For cross-sectional analysis of the printed tracks dicing was performed using a high-speed rotary saw (DISCO Corporation), equipped with a diamond blade (P1A863 SD6000N100BR50). To determine the powder deposition efficiency the weight of the sample substrate was measured before and after deposition and compared with previously calibrated powder feeding rates [16]. Prior to quality evaluation of the printed layer the sample was polished in order to remove partially sintered regions. For surface characterization a profilometer (Stylus Profilometer, KLA Tenors P7) was used.

4. Process parameters and results

The main process parameters we studied in this work include laser power, spot size and translation speed. Low power density can result in insufficient substrate melting and hence weak bonding and inclusions of not fully sintered glass. If the power density is too high, evaporation of the substrate and deposited material can occur, resulting in low deposition efficiency. In extreme case, the volume of evaporated material might be larger than the deposition rate. It is therefore important to study the evaporation rates in relation to the laser scanning parameters. Optimal conditions can be found between these two extremes but may vary depending on the size and geometry of the printed structure, mainly related to energy transfer to and from the build and thermal conduction within the material. The impact of different process parameters was examined by fabrication of different geometries such as trenches, tracks and larger structures consisting of multiple overlapping deposition tracks.

4.1. Material evaporation

To determine the evaporation kinetics of the LC system a dry run, i.e., without injecting glass powder, was performed at different laser power settings and scanning speeds. The laser spot size on the substrate was set to have a diameter of 1.20 mm, slightly larger than the diameter of the powder feeding nozzle. The laser beam was launched normal to the substrate, as shown in Fig. 7, with the tip of the nozzle positioned approximately 9 mm from the hot-zone. Although powder feeding was turned off in these experiments, dry air was injected at a flow rate of 4 L/min for both CG and SG, to include their cooling effect of the substrate. Laser power settings evaluated here was 33 W, 42.5 W and 50 W, while the scanning speed was varied between 0.1 mm/s to 11.5 mm/s. Linear translation of the substrate along the y-axis was triggered by opening the beam shutter. An example of the evaporation trenches formed when scanning the laser beam across the substrate is shown in Fig. 10(a). Figure 10(b) shows the corresponding transverse surface profile measured using the profilometer.

Here the line scan is performed at the middle section of the trenches to avoid start and end sections affected by the acceleration and deceleration of the stage. Based on the measured profile in Fig. 10(b) the volume of evaporated glass per mm was calculated, with the resulting plot shown in Fig. 10(c). Due their shape, depth of the trenches deeper than 100 µm could not be measured accurately with stylus profilometer.

4.2. Directional dependence while using a single, off-axis powder nozzle

When using a single off-axis powder feeding nozzle, the deposition efficiency during LC will depend on the relative movement between substrate and powder nozzle. In this sections we describe some of the main consequences. Consider the image of the powder feeding nozzle shown in Fig. 8(a). The *forward* direction is then defined as the relative movement of the nozzle in the direction of injected powder, i.e. the substrate moves to the right in Fig. 8(a). The *backward*

Optical Materials EXPRESS

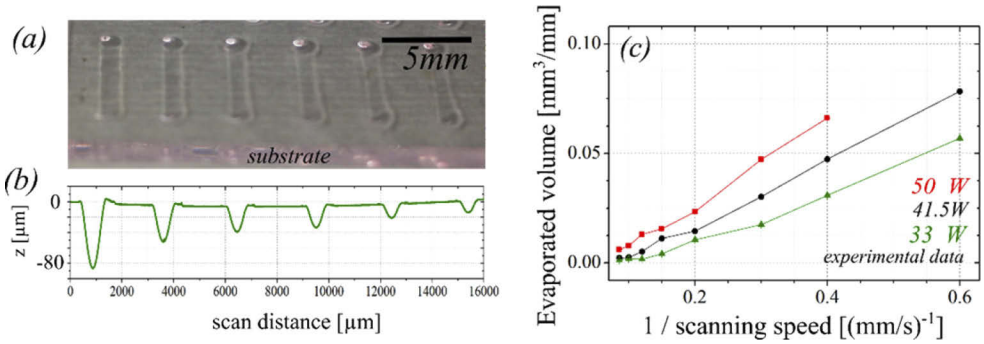

Fig. 10. Substrate with line trenches (a) formed by evaporation with corresponding surface profile (b), and calculated evaporation volume of as a function of scan speed and laser power (c).

direction is defined as the relative movement of the nozzle in opposite direction of injected powder, i.e., the substrate moves towards the left in Fig. 8(a). For these experiments fumed silica was added at a rate of 0.5 g/min with a CG and SG flow rate of 4 L/min, respectively. The laser power was set to $P_{max} = 45$ W with a substrate spot size of 1.2 mm, while the rate of substrate translation relative to the nozzle was set to $v_s = 380$ mm/min. After deposition, the samples were diced, and the cross sections were examined using an optical microscope. Typical results for forwards and backwards LC deposition are shown in Fig. 11.

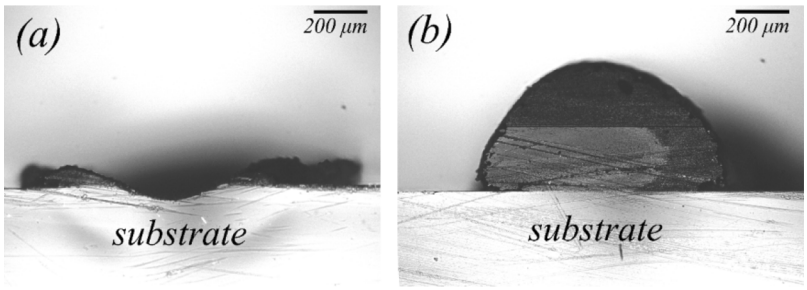

Fig. 11. Cross-sectional profiles of tracks printed in (a) forward direction and (b) backwards direction.

In the case of printing in the forward direction tracks were highly irregular with sections having very low amount of deposited glass, and even signs of evaporation trenches in the substrate, as indicated in Fig. 11(a). For backwards printed tracks continuous deposition of glass along the whole traversed length was observed, with a typical cross-sectional image shown in Fig. 11(b). When LC was performed in the forward direction the buildup of glass partially blocked the injected powder from reaching the melt pool, which can explain the irregular structure along the deposited track. When operating in the backwards direction, the deposited glass is located on the far side of the melt pool and will therefore not block the injected powder. The as-manufactured tracks are not optically transparent as the surface is partially covered with partially sintered powder, a typical feature of the powder-based LC.

4.3. Deposition efficiency

To evaluate the deposition efficiency a series of 6 mm long tracks were deposited in backwards direction with varying laser power and scan speed. Laser power settings evaluated here were

Optical Materials EXPRESS

33 W, 42.5 W and 50 W, while the scanning speed was varied between 0.1 mm/s to 11.5 mm/s. Powder injection was set at a constant feeding rate of 0.4 g/min with CG and SG flow rates set to 4 L/min. The tip of the powder feeding nozzle was positioned 9 mm from the center of the melt pool. Deposited tracks were diced and analyzed using an optical microscope. Figure 12(a) shows a series of single tracks, while Fig. 12(b) shows a profile image of deposited tracks.

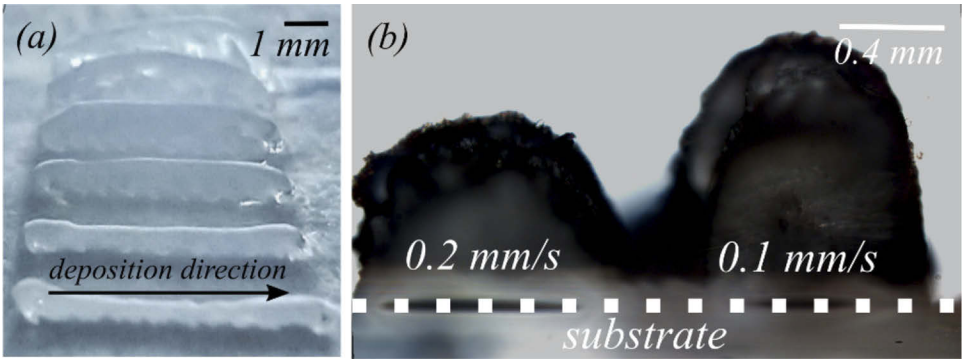

Fig. 12. Example (a) of a single-track deposition with (b) showing cross-sectional microscope image of two tracks.

With a backwards deposition in the range of 0.1–0.4 mm/s, a measured track thickness of approximately 1.4 mm (+/-0.1 mm) was obtained. The calculated volume of the deposited tracks, as a function of deposition speed, is shown in Fig. 13(a). The volume is given as mm^3 per unit length of 1 mm and was calculated from the cross-sectional area measured from microscope images. Due to stage acceleration and deceleration, cross-sectional images were taken from the mid-section of each track. An estimate of the powder deposition efficiency (η) was then calculated as the ratio of measured volume per unit length of the deposited glass to the volume of injected powder per unit length, having a known and fix powder feed rate during the deposition. The calculated deposition efficiency as a function of scanning speed is shown in Fig. 13(b).

Based on the data in Fig. 13(b) we have divided the experimental results into three different ranges; high-, intermediate-, and low-speed deposition. We define the scanning velocities (v_d) as; high-speed deposition for $v_d > 5$ mm/s, intermediate-speed for 1 mm/s $> v_d > 5$ mm/s and low-speed for $v_d < 1$ mm/s. The reduced deposition efficiency in the high-speed range is related to the reduced time of laser irradiation, providing insufficient heating of the melt pool. In the intermediate range a deposition efficiency of approximately 44% was achieved for a laser power of 50 W and a scan-speed of 2.5 mm/s. Reducing the scan-speed further results in a reduction of the deposition efficiency. In the low-speed range evaporation becomes severe (see Fig. 10(c)), effectively reducing the deposition efficiency. However, in the intermediate range, for scan speeds lower than 3.3 mm/s, printed tracks contained an increasing amount of partly sintered powder trapped below a fully melted layer (see Fig. 14(a)). A possible explanation for this effect is that the increased height of the track offsets the position of the melt pool from optimal alignment with the injected powder cone, as schematically described in Fig. 14(b). The effect is partial shadowing of the bottom section of the printed track, trapping partly sintered powder.

For deposition speeds above $v_d > 3.3$ mm/s the printed glass was fully melted and densified. In Fig. 15 an example of a cross-sectional image of a fully sintered track is shown. Here the printing speed was $v_d = 6.6$ mm/s with a powder feeding rate of 0.4 g/min and using a laser power of 47 W focused to a spot size of approximately 1.2 mm. A powder deposition efficiency of appr. 30% was measured by weighting the substrate before and after glass deposition. The printed track had a rough outer surface characteristic of powder-based techniques, while the inner section showed fully densified silica glass.

Optical Materials EXPRESS

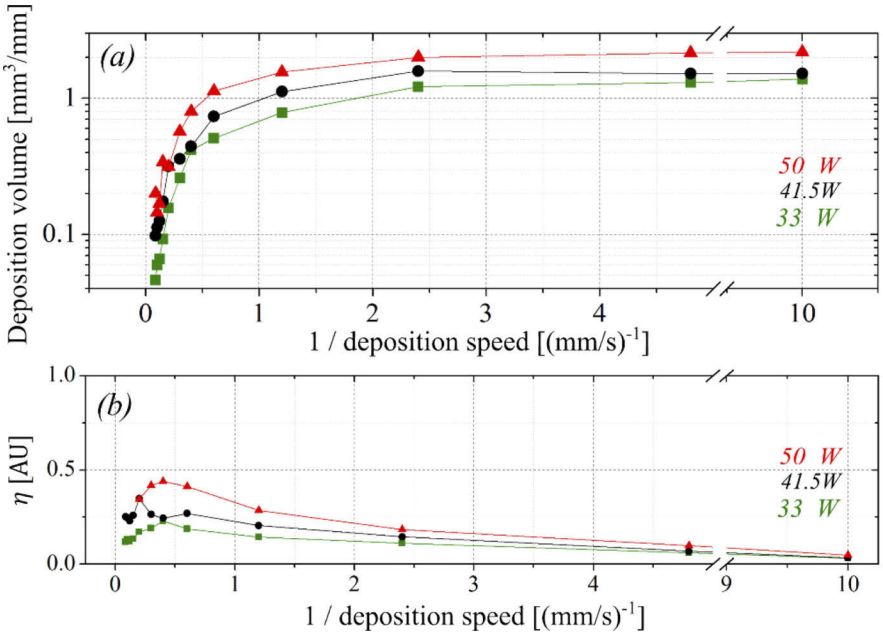

Fig. 13. Measured (a) printed glass volume in backwards deposition as a function of deposition speed measured using an optical microscope, while (b) shows the calculated normalized material efficiency.

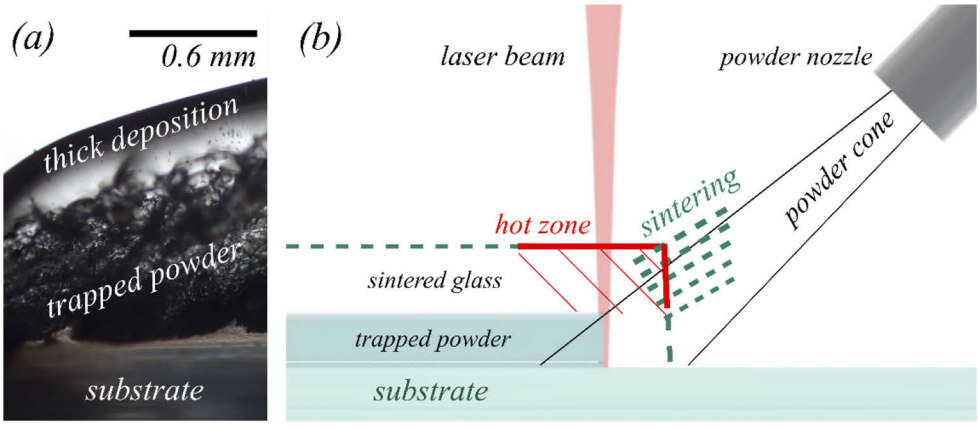

Fig. 14. Typical side view of thick deposition tracks (a) with partly sintered powder, trapped under sintered glass with a schematic (b) of deposition dynamics for low to intermediate deposition speed.

Optical Materials EXPRESS

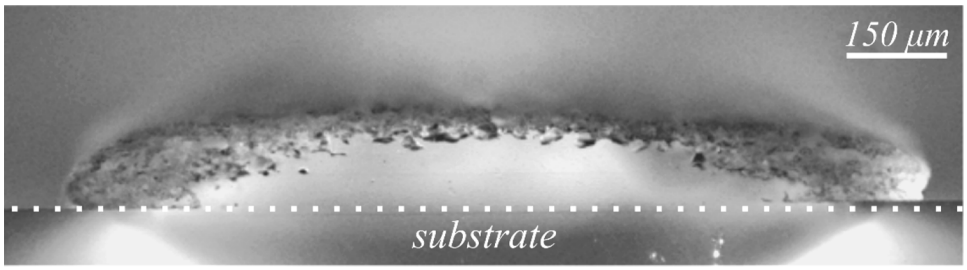

Fig. 15. Microscope image of diced sample with a printed track using a scanning speed of 6.6 mm/s.

4.4. Fused silica layers

Schematically shown in Fig. 16(a) is a sample consist of several tracks manufactured in backwards direction with a designed 20% track overlap (covered area of approx. 1 cm^2, powder feeding of 0.4 g/min, scanning speed of 6.6 mm/s, P_{max}=47 W). The top layer of partly sintered powder (see Fig. 16(b)) was removed from the sample by polishing, leaving the substrate with an approximately 100 μm thick layer of printed glass, see Fig. 16(c). Fully densified areas in the printed and polished layer showed thin periodic lines containing partially sintered glass, which is due to the partially overlapping lines during printing (in red, see Fig. 16(a)).

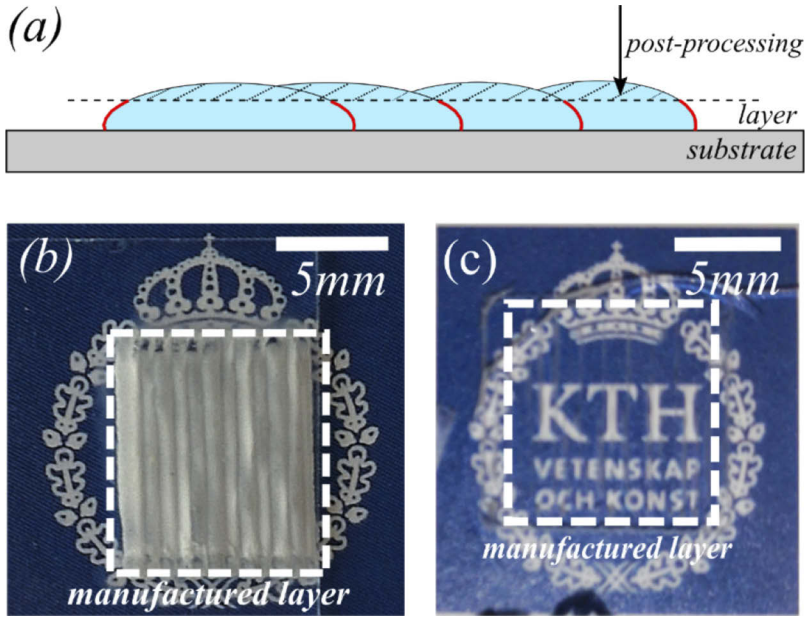

Fig. 16. Schematic (a) of the manufactured layer. Sample with (b) the as-printed layer placed on top of university logo showing the partly sintered surface, and (c) the same sample polished having a 100 μm thick transparent glass layer.

5. Conclusions

In this work we demonstrate a method for powder-based laser cladding of silica glass. We addressed the shadowing effect, which has been seen as a major limitation in obtaining fully dense sintered glass. By using a combination of a mid-IR laser and sub–micrometer powder it

Optical Materials EXPRESS

was possible to largely eliminate the shadowing effect. By reducing the particle size by an order of magnitude, compared to typically used powders, absorption as well as the scattering can be significantly reduced. Here we used a CO_2 laser operating at 10.6 µm, at which silica glass has very high absorption combined with fumed silica with particle size in the range of 0.1 - 0.05 µm had been used.

In order to handle fumed silica a modified powder delivery system was built. Additionally, a new injection nozzle design was developed with integrated shaping gas to obtain a semi-laminar flow at the nozzle exit, thereby enabling a longer working distance between the nozzle and the melt pool. The latter is important to minimize heating of the nozzle. Printing was performed by using the nozzle in a single off-axis configuration. Motorized and computer-controlled stages, using commercially available 3D printing firmware, enabled fast and repetitive printing in three dimensions. The system was evaluated, and deposition parameters were optimized to obtain inclusion free, fully sintered glass.

By using a 47 W CO_2 laser, with a scanning speed of 6.6 mm/s fully melted and densified glass was printed. Powder deposition efficiency of up to 30% was measured by weighing the substrate before and after deposition. During the process deposition rate up to 29 mm^3/min was achieved.

Partially sintered, not fully densified glass was located at the surface of the printed tracks. This is a characteristic of powder-based manufacturing methods, where regions with lower surface temperature results in incomplete sintering.

For multi-layer printing the partially sintered surfaces will lead to voids and imperfections within the glass matrix. These imperfections can be mitigated through intermediate post-processing by CO_2-laser surface melting. To address the directional dependence on printing, multiple co-axial printing nozzles can be used. Addressing these issues will significantly improve the quality of multilayer printing, enabling rapid prototyping, or manufacturing of a range of optical elements and devices, such as windows, waveguides, lenses, or fiber preforms.

Funding. Knut och Alice Wallenbergs Stiftelse (2016.0104); Stiftelsen för Strategisk Forskning (GMT14-0071, RMA150135).

Acknowledgments. We thank the Swedish Foundation for Strategic Research and the K.A. Wallenberg foundation for financial support and Laura Barett for help with the profilometer measurements.

Disclosures. The authors declare no conflicts of interest.

Data availability. Data underlying the results presented in this paper are not publicly available at this time but may be obtained from the authors upon reasonable request.

References

1. D.W. Rosen, B. Stucker, and I. Gibson, *Additive Manufacturing Technologies: 3D Printing, Rapid Prototyping, and Direct Digital Manufacturing* (Springer, 2010).
2. T. D. Ngo, A. Kashani, G. Imbalzano, K. T. Q. Nguyen, and D. Hui, "Additive manufacturing (3D printing): a review of materials, methods, applications and challenges," Composites, Part B **143**, 172–196 (2018).
3. I. W. Donald, B. L. Metcalfe, and R. N. J. Taylor, "The immobilization of high level radioactive wastes using ceramics and glasses," J. Mater. Sci. **32**(22), 5851–5887 (1997).
4. K. L. Wlodarczyk, D. P. Hand, and M. M. Maroto-Valer, "Maskless, rapid manufacturing of glass microfluidic devices using a picosecond pulsed laser," Sci. Rep. **9**(1), 20215 (2019).
5. J. Klein, M. Stern, G. Franchin, M. Kayser, C. Inamura, and S. Dave, "Additive manufacturing of optically transparent glass," 3D Print. Additive Manuf. **2**(3), 92–105 (2015).
6. P. von Witzendorff, L. Pohl, O. Suttmann, P. Heinrich, A. Heinrich, J. Zander, H. Bragard, and S. Kaierle, "Additive manufacturing of glass: CO_2-Laser glass deposition printing," Procedia CIRP **74**, 272–275 (2018).
7. M. Fateria, A. Gebhardta, S. Thuemmlera, and L. Thurna, "Experimental investigation on selective laser melting of glass," Phys. Procedia **56**, 357–364 (2014).
8. F. Kotz, K. Arnold, W. Bauer, D. Schild, N. Keller, K. Sachsenheimer, T. M. Nargang, C. Richter, D. Helmer, and B. E. Rapp, "Three-dimensional printing of transparent fused silica glass," Nature **544**(7650), 337–339 (2017).
9. E. Toyserkani, A. Khajepour, and S. F. Corbin, *Laser Cladding*, (CRC, 2005).
10. J. Luo, H. Pan, and E. C. Kinzel, "Additive manufacturing of glass," J. Manuf. Sci. Eng. **136**(6), 061024 (2014).
11. G. Marchelli, D. Storti, M. Ganter, and M. Prabhakar, "An Introduction to 3D Glass Printing," *Solid Freeform Fabrication Symposium Proceedings*, Austin, TX, Aug. 3–5, pp. 95–107 (2010).

Optical Materials EXPRESS

12. Y. Pei and J. T. M. De Hosson, "Functionally graded materials produced by laser cladding," Acta Mater. **48**(10), 2617–2624 (2000).
13. R. Comesaña, F. Lusquiños, J. del Val, M. López-Álvarez, F. Quintero, A. Riveiro, M. Boutinguiza, A. de Carlos, J. R. Jones, R. G. Hill, and J. Pou, "Three-dimensional bioactive glass implants fabricated by rapid prototyping based on CO_2 laser cladding," Acta Biomater. **7**(9), 3476–3487 (2011).
14. Y. L. Huang, G. Y. Liang, J. Y. Su, and J. G. Li, "Interaction between laser beam and powder stream in the process of laser cladding with powder feeding," Model. Simulat. Mater. Sci. Eng. **13**(1), 47–56 (2005).
15. R. Comesaña, F. Quintero, F. Lusquiños, M. J. Pascual, M. Boutinguiza, A. Durán, and J. Pou, "Laser cladding of bioactive glass coatings," Acta Biomater. **6**(3), 953–961 (2010).
16. P. Maniewski, F. Laurell, and M. Fokine, "Reduction of shadowing effect during laser cladding of fused silica glass using sub-micron powders," Proc. SPIE **11677**, 1167711 (2021).
17. G. Marchelli, R. Prabhakar, D. Storti, and M. Ganter, "The guide to glass 3D printing: developments, methods, diagnostics and results," Rapid Prototyping J. **17**(3), 187–194 (2011).
18. Y. Tang, J. Y. H. Fuh, H. T. Loh, Y. S. Wong, and L. Lu, "Direct laser sintering of a silica sand," Mater. Des. **24**(8), 623–629 (2003).
19. R. Kitamura, L. Pilon, and M. Jonasz, "Optical constants of silica glass from extreme ultraviolet to far infrared at near room temperature," Appl. Opt. **46**(33), 8118–8133 (2007).
20. J. Lin, "Laser attenuation of the focused powder streams in coaxial laser cladding," J. Laser Appl. **12**(1), 28–33 (2000).
21. G. Mie, "Contributions to the optics of diffuse media, especially colloid metal solutions," Ann. Phys. **330**(3), 377–445 (1908).
22. H.C. van de Hulst, *Light Scattering by Small Particles*, (Wiley, 1957).
23. W.J. Wiscombe, "Mie scattering calculations: advances in technique and fast, vector-speed computer codes", Boulder, National Center for Atmospheric Research, (1979).
24. S. Prahl, *miepython v1.3.0*, (2017), https://github.com/scottprahl/miepython, accessed: June 2020
25. M. Kerker, *The Scattering of Light and Other Electromagnetic Radiation* (Academic, 1969), Chap. 3.